# Smart pH-Sensitive and Temporal-Controlled Polymeric Micelles for Effective Combination Therapy of Doxorubicin and Disulfiram

Xiaopin Duan,[†,‡,§] Jisheng Xiao,[†,§] Qi Yin,[†] Zhiwen Zhang,[†] Haijun Yu,[†] Shirui Mao,[‡] and Yaping Li[†,*]

[†]Center of Pharmaceutics, Shanghai Institute of Materia Medica, Chinese Academy of Sciences, Shanghai 201203, China, and [‡]School of Pharmacy, Shenyang Pharmaceutical University, Shenyang 110016, China. [§]These authors contributed equally to this work.

**ABSTRACT**
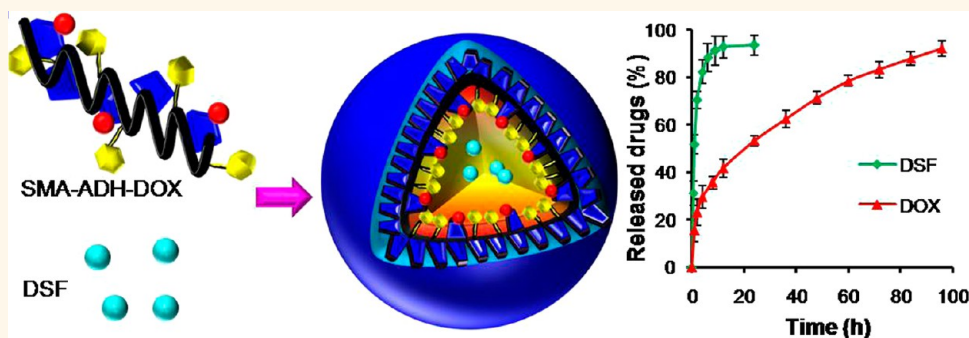


The combination of a chemotherapeutic drug with a multidrug resistance (MDR) modulator has emerged as a promising strategy for treating MDR cancer. To ensure two drugs could be simultaneously delivered to tumor region at the optimum ratio, and the MDR modulator could be released earlier and faster than the chemotherapeutic drug to inactivate P-glycoprotein (P-gp) and subsequently inhibit the pumping out of the chemotherapeutic drug, a smart pH-sensitive polymeric micelles system with high drug loading and precise drug ratio was designed and prepared by conjugating doxorubicin (DOX) to poly(styrene-co-maleic anhydride) (SMA) derivative with adipic dihydrazide (ADH) through a acid-cleavable hydrazone bond, and then encapsulating disulfiram (DSF), a P-gp inhibitor as well as an apoptosis inducer, into the micelles formed by the self-assembly of SMA-ADH-DOX (SAD) conjugate. The pH-sensitive polymeric micelles system enabled a temporal release of two drugs: encapsulated DSF was released fast to inhibit the activity of P-gp and restore cell apoptotic signaling pathways, while conjugated DOX was released in a sustained and pH-dependent manner and highly accumulated in drug resistant cells to exert therapeutic effect, due to the inactivation of P-gp by DSF. The smart co-delivery system was very effective in enhancing the cytotoxicity by increasing the intracellular accumulation of DOX and promoting the apoptotic response, and showed the most effective inhibitory effect on the growth of drug-resistant breast cancer xenografts as compared to other combinations of both drugs. In a word, this smart co-delivery system has significant promise for the clinical therapy of MDR cancer.

**KEYWORDS:** combination therapy · multidrug resistance · pH-sensitive · polymeric micelles · doxorubicin · disulfiram · temporal release

T he combination therapy has been adopted in clinics as a primary cancer treatment regimen. On the one hand, the combination of multiple drugs with different molecular targets can delay the cancer adaptation process, thereby reducing the possibility of cancer cell mutations. On the other hand, the co-administration of multiple drugs that target the same cellular pathway can function synergistically for better therapeutic efficacy with higher target selectivity.[1,2] Unfortunately, the current combination therapies are far from perfect. The varying pharmacokinetics, biodistribution and membrane transport properties among different drug molecules, which will result in inconsistent drug uptake and suboptimal drug combination at the tumor site, make dosing and scheduling optimization extremely difficult.[3,4] These challenges drive scientists to find the new, clever and elegant approaches for cancer

treatment by incorporating nanotechnology with combination therapy.

The combination of multiple agents within a single nanocarrier can guarantee the simultaneous delivery of drugs, and provide advantages over the combination of the single administration of the free drugs. The multiagent systems should have high drug loading and precise drug ratio to ensure sufficient amount of drugs delivered to tumor site at optimum ratio. Another requirement for multiagent nanocarriers is to remain stable in the blood circulation and specifically release drugs at the tumor site to maximally exert their antitumor activities and reduce side effects.[5,6] Furthermore, for reversal of multidrug resistance (MDR), the modulator should be released earlier and faster than the chemotherapeutic drug to inactivate drug efflux pumps in advance and then inhibit the pumping out of the chemotherapeutic drug. However, the present approaches for combination therapy are the noncovalent encapsulation of two drugs in a single nanocarrier, which can result in poor stability and batch-to-batch variability in drug loading and release kinetics, especially when two drugs possess different solubility, charge and molecular weight. In addition, the encapsulation of hydrophilic drugs could result in low drug loading and encapsulation efficiency.[7,8]

To resolve above problems, here we designed a smart pH-sensitive polymeric micelles system with high drug loading and precise drug ratio to co-deliver the hydrophilic doxorubicin (DOX) and the hydrophobic disulfiram (DSF) (a P-gp inhibitor and apoptosis inducer) in a temporal release manner to restore apoptotic signaling pathways and overcome MDR. At first, DOX was conjugated to poly(styrene-co-maleic anhydride) (SMA) derivative with adipic dihydrazide (ADH) through an acid-cleavable hydrazone bond, and then DSF was encapsulated into the micelles formed by the self-assembly of SMA-ADH-DOX (SAD) conjugate. The DSF-loaded SAD micelles (DSM) enabled a temporal release of two drugs: encapsulated DSF was released fast to inhibit the activity of P-gp and restore cell apoptotic signaling pathways, while the conjugated DOX was released in a sustained and pH-dependent manner and highly accumulated in cancer cells to exert therapeutic effect. The potency of this smart co-delivery system in reversing MDR was evaluated in DOX-resistant breast cancer cells (MCF-7/ADR cells) and in MCF-7/ADR tumor-bearing mice. It was expected that the combination therapy could promote synergistic actions and deter the development of cancer resistance.

## RESULTS AND DISCUSSION

**Synthesis and Characterization of SAD Conjugate.** The aim of this work was to design and develop acid-cleavable SAD micelles to co-deliver DOX and DSF into tumor tissue and overcome MDR. To avoid the steric hindrance and introduce the hydrazide groups into the backbone, SMA was first derivatized with ADH, and then, DOX was conjugated to the pendant hydrazide groups of SMA-ADH (SA) via an acid-sensitive hydrazone bond (Figure S1). The conjugation was then confirmed by $^1$H NMR spectra and UV scanning spectra. The presence of the characteristic resonances of styrene residue of SMA (6.8−7.4 ppm) and DOX (4.3, 5.1, 5.45, 7.6, 7.85, and 8.0 ppm) in the $^1$H NMR of SAD indicated that the conjugate was successfully synthesized (Figure S2). In the UV scanning spectra (Figure S3), SA showed no absorption in the range of 600−400 nm, while SAD exhibited a broad absorption peak, which was indentified with free DOX, confirming the successful synthesis of SAD conjugate. Elemental analysis showed that approximately 88.2% of maleic anhydride was reacted with ADH, while about 23.2% of the grafted ADH was further reacted with DOX (Table S1). Furthermore, the content of DOX in SAD conjugate determined by fluorescence spectrophotometry was as high as 25% (w/w).

The hydrazone linker was hydrolytically cleavable, particularly at low pH values, and the hydrolysis rate was negatively related to the pH value. As shown in Figure S4, SAD exhibited a monodispersed peak at 11.5 min when analyzed by high performance liquid chromatography (HPLC), while free DOX was eluted at 2.7 min. The incubation of SAD at low pH values for 2 h led to partial degradation of the hydrazone bonds, resulting in two separate elution peaks, corresponding to DOX and SAD, respectively. Additionally, the hydrolysis rate accelerated with the decrease of pH value, suggesting that the smart polymeric micelles designed here was pH-sensitive.

**Preparation and Characterization of DSM.** The synthesized SAD conjugate could self-assemble into micelles in an aqueous solution with a small particle size of 88.58 ± 4.12 nm and a narrow distribution, determined by dynamic light scattering (DLS). In addition, SAD exhibited a negative zeta potential of −22.8 mV, which might due to the higher amount of carboxyl groups on the micelles surface than that of hydrazide groups (Figure S5A). The transmission electron microscopy (TEM) image showed that the micelles were generally in spherical shape with good monodispersity (Figure S5B). Furthermore, SAD micelles displayed high drug loading capacity for the MDR modulator DSF (drug loading content up to 5%). The DSF-encapsulated micelles also exhibited spherical morphology with no appreciable change of particle size and zeta potential in comparison with blank micelles, implying a good stability of the nanosystem (Figure 1A,B). The particle size of micelles was beneficial for tumor-targeting delivery, which was large enough to avoid renal filtration and small enough to penetrate through the leaky vasculatures in tumor region, while reducing reticuloendothelial system (RES)-mediated clearance.[9]

The in vitro colloidal stability of micelles was evaluated in the presence of bovine serum albumin (BSA), which is known as an amphiphile trap that disrupts
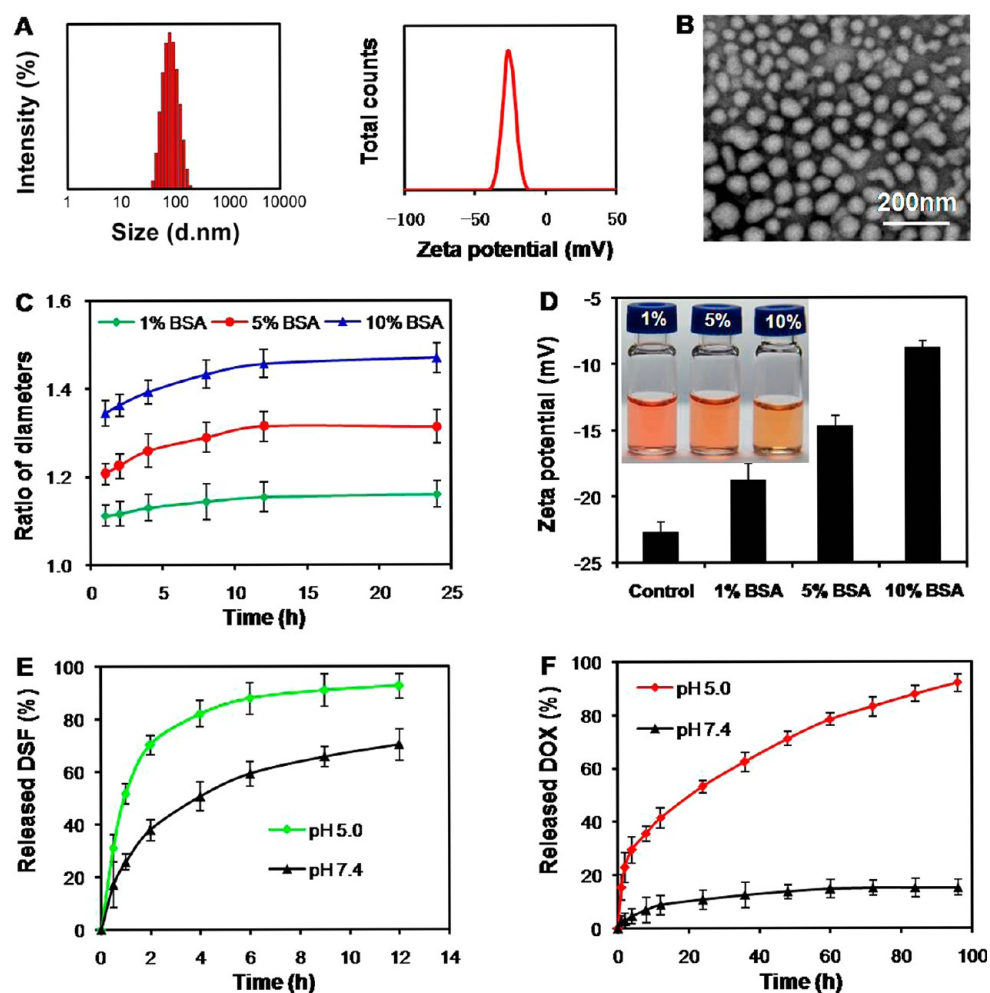
**Figure 1.** (A) Size distribution and zeta potential of DSM determined by DLS. (B) TEM image of DSM. (C) Time-dependent colloidal stability of DSM in water containing 1%, 5% and 10% BSA at 37 °C. The ratio of diameters is the ratio between the time-dependent hydrodynamic diameter and the initial hydrodynamic diameter in water. (D) Zeta potential changes of DSM after incubation with 1%, 5% and 10% BSA at 37 °C for 24 h. Inset: photographs of DSM after incubation with BSA at 37 °C for 24 h. (E and F) Time-dependent cumulative release of DSF (E) and DOX (F) from DSM at different pH values.

micellar nanocarriers.[10] SAD and DSM were diluted in water containing various concentrations of BSA at 37 °C, and the time-dependent changes in hydrodynamic diameter were determined by DLS. The particle size increased with BSA concentration and incubation time increasing (Figure 1C and Figure S5C). Both micelles were very stable in water containing 1% BSA, and no significant size change was observed after even 24 h incubation. When the concentration of BSA increased to 5% (the physiological concentration of BSA),[11] the hydrodynamic size of micelles increased to about 1.3-fold of the original size after 24 h aging at 37 °C, but the particles still exhibited good dispersibility. Even when the concentration of BSA was as high as 10%, there was still no visible particle precipitation observed for both micelles. In addition, the incubation of micelles with BSA led to an increase of the zeta potential (Figure 1D and Figure S5D), which might be due to the relatively low pH value of micellar solution (pH ~4.5), resulting from the presence of more carboxyl groups than hydrazide groups on the surface. At this pH, BSA had a slight positive charge, and the absorption of BSA

on micelles surface would neutralize and shield the negative charge of micelles, leading to an increase of the zeta potential. Additionally, the nearly neutral charge of BSA could reduce its interaction with micelles, thereby decreasing the amount of BSA that absorbed to micelles surface. Furthermore, at the physiological environment, BSA would have a net negative charge, which could further reduce its absorption to negatively charged surface of micelles, resulting in high stability of the micelles, and then prolonged circulation time.[12]

DSM was expected to enable a temporal release of two drugs: DSF was fast released to inhibit the activity of P-gp, and DOX was released in a sustained manner in response to endosomal pH environment and highly accumulated in cells, achieving selective and efficient intracellular drug release and finally reversing MDR. To demonstrate this potential, the release kinetic for each drug was quantified. As presented in Figure 1E, DSF showed a fast release, 92.6% and 70.2% of DSF were released within 12 h incubation at pH 5.0 and 7.4, respectively. The fast release of DSF could guarantee

the quick inactivation of P-gp, and subsequently the high accumulation of DOX in cells. In contrast, the release of DOX was found to be significantly slower in buffer solution that models the blood environment (pH 7.4 at 37 °C), and only a slight release (up to 15.3%) was observed within 96 h incubation, while the release of DOX became fast in a buffer that simulates the condition in the endosomes of target cells (pH 5.0 at 37 °C), and 92.1% of DOX was released from the micelles within 96 h incubation in a sustained manner (Figure 1F). This pH-dependent release behavior was highly desirable for targeted cancer therapy because it could significantly minimize the amount of premature drug release during circulation in the bloodstream, yet provide a sufficient amount of drug to effectively kill the cancer cells once the micelles were internalized through endocytic pathways.

**DOX Accumulation and Efflux Assay.** DSF has been reported to can inhibit P-gp activity *in vitro* by covalently modifying cysteine residues within the nucleotide-binding domains and/or by blocking its maturation, leading to an increased intracellular accumulation of cytotoxic drugs.[13,14] The effect of DSF on the intracellular accumulation and efflux of DOX was performed in DOX-resistant MCF-7/ADR cells and DOX-sensitive MCF-7 cells. As expected, free DOX accumulation in MCF-7/ADR cells was extremely low, even incubation for 4 h, but significantly increased when co-incubation with DSF was used due to the inhibitory effect of DSF on P-gp. SAD and DSM could be internalized into the cells through endocytic pathways like other nanocarriers and counteracted the effect of P-gp mediated drug efflux, leading to high cellular accumulation (Figure 2A). On the contrary, as a result of the low expression of P-gp, the accumulation of all DOX formulations in MCF-7 cells was relatively high and increased with prolongation of incubation time (Figure 2B).

In drug efflux assay, cells were first cultured with free DOX, a mixture of free DOX and DSF (DOX + DSF), SAD, a mixture of SAD and DSF (SAD + DSF) or DSM for 4 h, and then incubated with fresh medium for different time. The amount of DOX retained in cells was determined by FACSCalibur system. The results showed that the content of DOX was very low in free DOX solution treated MCF-7/ADR cells and continuously decreased within the subsequent incubation as a result of efflux effect of P-gp. When DOX was combined with DSF, its concentration in cells was significantly higher and showed no obvious decrease. Similarly, the amount of intracellular DOX was also decreased in MCF-7/ADR cells treated by SAD as incubation time increased, due to the pumping out of DOX by P-gp after being released from the conjugate, and the decrease was markedly prevented by the addition of DSF. While in DSM treated MCF-7/ADR cells, the intracellular concentration of DOX was highest and the downward trend was slowest (Figure 2C). In MCF-7 cells, the DOX concentration in the beginning stage of the test was remarkably higher

than that in MCF-7/ADR cells, and no significant changes were seen within 4 h incubation (Figure 2D).

**Subcellular Localization.** The localization of DOX in cells was additionally observed by confocal microscopy. In MCF-7/ADR cells (Figure S6), free DOX showed little sign of uptake and mainly located around the cell membrane after 4 h incubation, due to the efflux effect of P-gp. The addition of DSF significantly increased the uptake of DOX, as indicated by the presence of higher red fluorescence intensity. Although SAD could increase the cellular uptake through bypassing drug efflux pumps, a part of DOX was found to colocalize with cell membrane, which could be because of the pumping out by P-gp after being released from SAD. In contrast, cells treated with SAD + DSF and DSM not only showed high red fluorescence intensity, but also reduced the amount of DOX colocalized with cell membrane. In MCF-7 cells (Figure S7), the red fluorescence intensity in cells incubated with DOX alone was comparable to that exposed to DOX in combination with DSF, indicating that DSF did not affect the uptake of DOX due to the low expression of P-gp in MCF-7 cells. Cells cultured with SAD, SAD + DSF and DSM only showed slightly higher red fluorescence intensity compared with that treated with DOX. In addition, no obvious red fluorescence was observed in cell membrane surrounding, indicating the absence of DOX colocalized with cell membrane. Interestingly, DOX internalized into cells was localized in cytoplasm around the nucleus in MCF-7/ADR cells for all DOX formulations after incubation for 4 h, while DOX could easily enter into nucleus in MCF-7 cells. Three-dimensional (3D) confocal microscopic images displayed a similar fluorescence profile (Figure 2E,F, Figure S8 and Figure S9). DOX was excluded from nucleus in MCF-7/ADR cells, on the contrary, most of DOX entered nucleus in MCF-7 cells. Since one of the pharmacological mechanisms of DOX was to inhibit the synthesis of nucleic acid through inserting into the nucleic acid after entrance into nucleus, the prevention for the nuclear localization of DOX could be one of MDR mechanisms.

It was reported that the entrance of free DOX into cells was accomplished by passive diffusion without the requirement for a specific transporter as following, DOX first bound to anionic phospholipids in membrane *via* electrostatic interaction, then entered cells through a flip-flop mechanism between the two membrane leaflets.[15,16] However, in drug resistant cells, internalized DOX was generally trapped in intracellular organelles and then extruded from cells by P-gp.[17] The long residence-time of the drug in the inner leaflet of the plasma membrane allowed P-gp a better opportunity to remove it from the cells.[18] For nanocarriers, endocytic pathways were the main mechanism for cellular internalization after binding to cell surface, which could bypass the drug efflux pumps and subsequently increase cellular uptake.[19−21] For example,
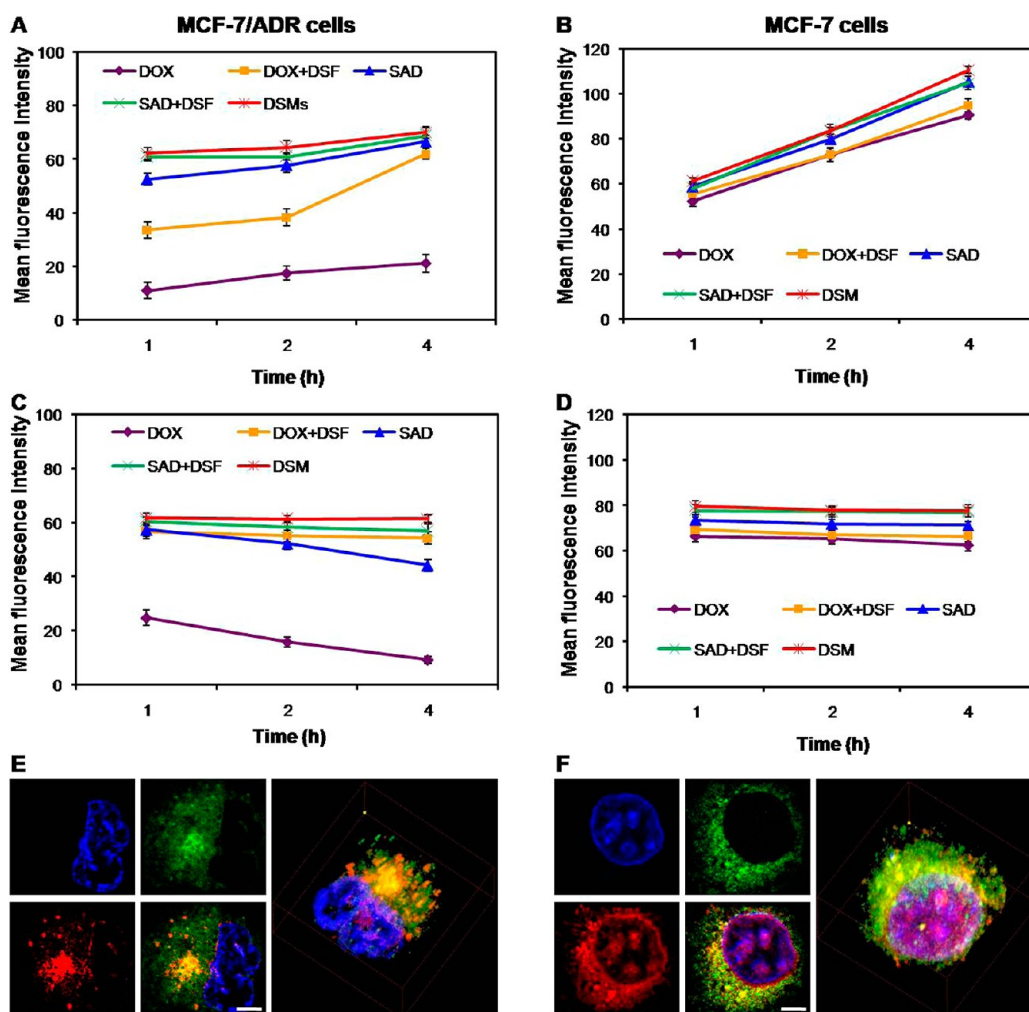
**Figure 2.** (A and B) The accumulation of DOX in MCF-7/ADR cells (A) and MCF-7 cells (B) after incubation with DOX, DOX + DSF, SAD, SAD + DSF and DSM for different time. (C and D) The efflux of DOX from MCF-7/ADR cells (C) and MCF-7 cells (D). Cells were first treated with DOX, DOX + DSF, SAD, SAD + DSF and DSM for 4 h, and then incubated with fresh medium for various times. (E and F) 2D and 3D confocal microscopic images of MCF-7/ADR cells (E) and MCF-7 cells (F) after culturing with DSM for 4 h. Nucleus and lysosome were stained by Hoechst 33342 and LysoTracker Green, respectively. (Scale bar: 5 $\mu$m).

both caveolae- and clathrin-mediated endocytosis were involved in the internalization of DOX-Hyd@AuNPs into MCF-7/ADR cells.[22] The confocal microscopic images of MCF-7/ADR cells shown in Figure 2E and Figure S8 revealed that the red fluorescence from DOX was mainly localized in the acidic organelles labeled with Lysotracker Green (green) after 4 h incubation, indicating the involvement of endocytic pathways. The localization in the acidic organelles was probably the prerequisite for the triggered intracellular drug release *via* the breakage of hydrazone bonds.

**In Vitro Cytotoxicity.** The cytotoxicity of various drug formulations was investigated by 3-(4,5-dimethylthia-zol-2-yl)-2,5-diphenyltetrazolium bromide (MTT) assay and the IC$_{50}$ value (the concentration that inhibited cell growth by 50%) was calculated simultaneously (Figure 3A,B and Table S2). The reduction of MTT is thought to mainly occur in the mitochondria through the action of succinate dehydrogenase, therefore providing a measure of mitochondrial function.[23] In MCF-7/ADR cells,

as a result of highly overexpression of P-gp, the IC$_{50}$ value of free DOX was as high as 0.32 mg/mL, which was ~480-fold resistant to DOX in comparison with the parent MCF-7 cells (IC$_{50}$ = 6.73 × 10$^{-4}$ mg/mL). After conjugation to SMA, the cytotoxicity of DOX was highly increased by 37.2-fold, due to high cellular uptake. When DSF was added, the cytotoxicity of DOX was further increased as a result of increased DOX inter-cellular accumulation and the apoptosis-promoting effect of DSF. The IC$_{50}$ values of DOX + DSF, SAD + DSF and DSM in MCF-7/ADR cells were 51.4-, 65.5-, and 89.7-fold less than that incubated with free DOX solution, respectively. In MCF-7 cells, DOX could be internalized easily and accumulated in cells at high level due to low expression of P-gp, thereby resulting in high cytotoxicity. The conjugation of DOX to SMA resulted in no obvious increase in the cytotoxicity of DOX. However, when DOX was combined with DSF, its cytotoxicity was increased, which could be due to the effect of DSF on cell apoptosis. The IC$_{50}$ values of DOX
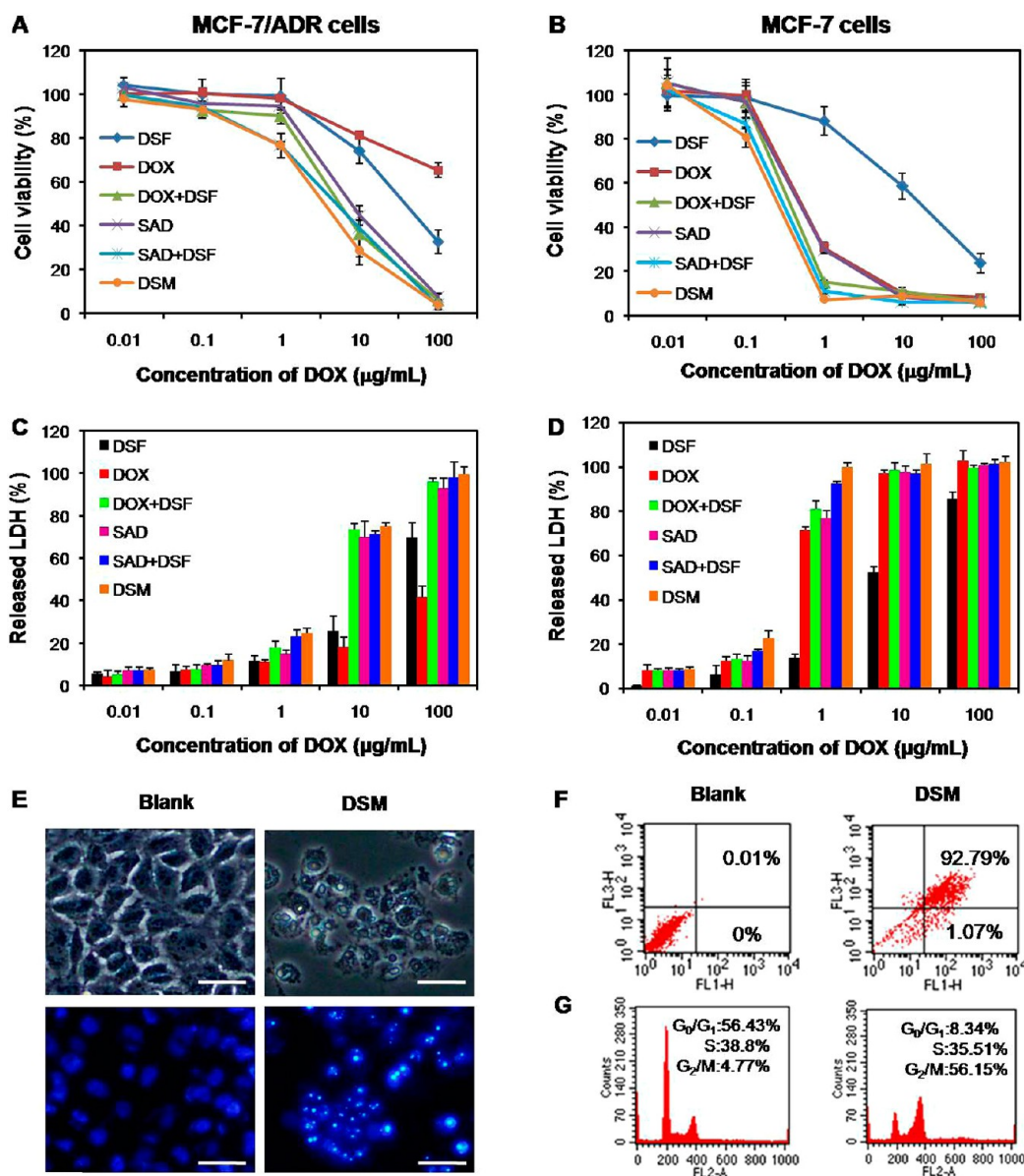
**Figure 3.** (A and B) Viability of MCF-7/ADR cells (A) and MCF-7 cells (B) after treatment with DSF, DOX, DOX + DSF, SAD, SAD + DSF and DSM at different concentrations for 48 h. (C and D) LDH released from MCF-7/ADR cells (C) and MCF-7 cells (D) exposed to DSF, DOX, DOX + DSF, SAD, SAD + DSF and DSM at different concentrations for 48 h. (E) The cellular and nuclear morphology of MCF-7/ADR cells after treatment with DSM for 48 h. (Scale bar: 50 $\mu$m). (F and G) Flow cytometry analysis for apoptosis (E) and cell cycle change (G) of MCF-7/ADR cells induced by DSM.

in DOX + DSF-, SAD + DSF-, and DSM-incubated cells were 1.48-, 2.23-, and 2.90-fold less than that treated with DOX solution, respectively.

The cytotoxicity of various formulations was verified by lactate dehydrogenase (LDH) release assay, an indicator of plasma membrane damage. The data of LDH release assay were well coordinated with MTT assay (Figure 3C,D and Table S3). In MCF-7/ADR cells, conjugation to SMA and combination with DSF all significantly elevated the levels of LDH release when compared with free DOX. The LD$_{50}$ (median lethal dose) of DOX + DSF, SAD, SAD + DSF and DSM showed 74.8-, 53.4-, 82.8-, and 98.8-fold decrease, respectively, compared with that treated with DOX solution. However, the increase of

LDH release in MCF-7 cells induced by DOX + DSF, SAD, SAD + DSF and DSM was not as remarkable as that in MCF-7/ADR cells, showing only 1.52-, 1.10-, 2.24-, and 2.99-fold increase, respectively, when compared with free DOX. The high cytotoxicity of DSM in MCF-7/ADR cells indicated that the multifunctional delivery system for the combination of chemotherapeutic agents and MDR modulators could significantly overcome MDR.

**Cell Apoptosis and Cell Cycle Assay.** It has been reported that DSF could induce cell apoptosis through different mechanisms including the inhibition of proteasome activity, the prevention of NF-$\kappa$B translocation, and the induction of reactive oxygen species generation,[24−27] thereby synergistically enhancing the *in vitro* cytotoxicity
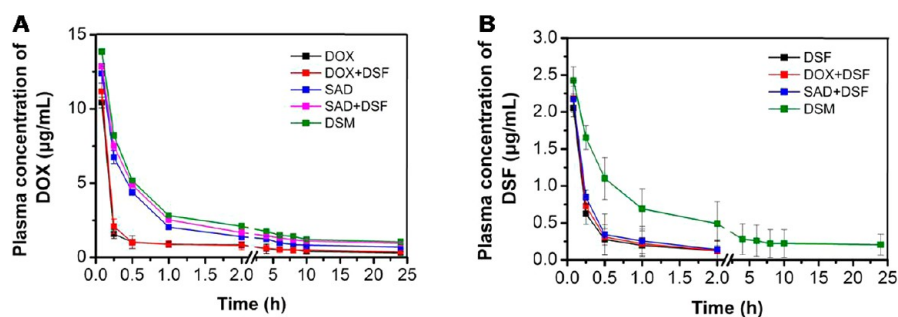
**Figure 4.** (A and B) Plasma concentration−time profiles of DOX (A) and DSF (B) in rats after intravenous administration of various drug formulations at the dose of 10 mg DOX/kg and 2 mg DSF/kg.

and apoptotic effect of chemotherapeutic drugs, such as 5-fluorouracil,[28] gemcitabine[29,30] and DOX.[31] In this work, it was demonstrated that DSF could increase intracellular accumulation and decrease efflux of DOX in MCF-7/ADR cells through inhibiting P-gp activity. Thus, the synergistic effect of DOX and DSF on cell apoptosis was evaluated. As indicated in Figure 3E and Figure S10A, MCF-7/ADR cells exposed to DOX alone did not show any visible apoptosis characters after 48 h incubation, and the conjugation could enhance the apoptotic effect of DOX through increasing its cellular uptake, while DSF alone could induce cell apoptosis, and the combination with DOX significantly increased the apoptotic effect. Most of cells appeared to have apoptotic morphology after treatment with DOX + DSF, SAD + DSF and DSM, as shown by marked changes in cellular and nuclear morphology, including chromatin condensation, membrane blebbing, nuclear breakdown, and the appearance of membrane-associated apoptotic bodies. The apoptotic cells were further quantified by prodium iodide (PI)/Annexin V staining and flow cytometric analysis (Figure 3F and Figure S10B). DOX showed high synergistic effect with DSF on promoting cell apoptosis, resulting in 42.6-, 47.3-, and 48.9-fold increase in number of apoptotic cells for DOX + DSF-, SAD + DSF-, and DSM-treated cells, compared with free DOX-treated cells.

DOX could insert into the minor grooves of nucleic acids to inhibit their synthesis, and finally change the cell cycle.[32] Figure 3G and Figure S10C showed that cells treated with DSF or DOX alone exhibited similar cell cycle with control cells, while DOX significantly changed the cell cycle after combination with DSF or conjugation to SMA, resulting in 64.9% and 63.7% reduction in the percentage of $G_0/G_1$ phase, and 8.1- and 7.8-fold increase in the percentage of $G_2/M$ phase, respectively. In addition, the conjugate could further change cell cycle when combination with DSF, as a result of higher DOX accumulation in cells. After incubation with SAD + DSF and DSM, the percentage of $G_0/G_1$ phase was reduced by 83.5% and 85.2%, and the percentage of $G_2/M$ phase was increased by 10.2- and 10.8-fold, respectively.

***In Vivo* Pharmacokinetics.** The mean DOX plasma concentration as a function of time following intravenous

administration of DOX, DOX + DSF, SAD, SAD + DSF and DSM was illustrated in Figure 4A, and the pharmacokinetic parameters, obtained by fitting the data to a two-compartment model, were summarized in Table S4. Significant differences in pharmacokinetic profiles were observed for free DOX and DOX conjugates. Free DOX was quickly removed from the circulating system after intravenously administration, showing a biphasic pattern with a rapid distribution phase ($t_{1/2\alpha} = 0.04$ h) and a rapid terminal elimination phase ($t_{1/2\beta} = 7.75$ h), and the addition of free DSF showed no obvious effect on the pharmacokinetic profile of free DOX. However, DOX conjugates, including SAD, SAD + DSF and DSM, all significantly changed DOX pharmacokinetic parameters in comparison with free DOX, as indicated by significantly higher area under the curve ($AUC_{0-\infty}$), elimination half-life ($t_{1/2\beta}$), mean residence time ($MRT_{0-\infty}$), and significantly lower total clearance (CL). Specifically, the $AUC_{0-\infty}$, $t_{1/2\beta}$ and $MRT_{0-\infty}$ for DSM were 70.52 $\mu$g·h/mL, 23.82 h and 47.60 h, which were 5.77-, 3.07-, and 5.59-fold higher than that of free DOX, respectively, while CL for DSM was 3.98-fold lower than that of free DOX, implying a longer retention of the drug in blood circulation.

The concentration−time curve of DSF after administration of DSF, DOX + DSF, SAD + DSF and DSM was illustrated in Figure 4B, and the pharmacokinetic parameters were summarized in Table S5. The plasma concentration of DSF in rats injected with free DSF significantly decreased over time, and was below the HPLC detection limit after 2 h. The $AUC_{0-\infty}$, $t_{1/2\beta}$ and $MRT_{0-\infty}$ for free DSF were only 1.05 $\mu$g·h/mL, 1.60 h and 1.25 h, respectively, while the CL for free DSF was as high as 1519.70 mL/(h·kg). On the contrary, DSM significantly slowed the decrease of the plasma concentration of DSF, showing a higher $t_{1/2\beta}$ (29.79 h) with a higher $AUC_{0-\infty}$ (15.95 $\mu$g·h/mL). The increased blood circulation time of DSF by DSM was also evidenced by the increase of $MRT_{0-\infty}$ (45.25 h) and the decrease of CL (143.52 mL/(h·kg)) in comparison with free DSF. The long systemic circulation time and slow plasma elimination rate of DSM were probably due to their low protein absorption and high colloidal stability, which could reduce the clearance rate by RES, thereby prolonging blood circulation time.
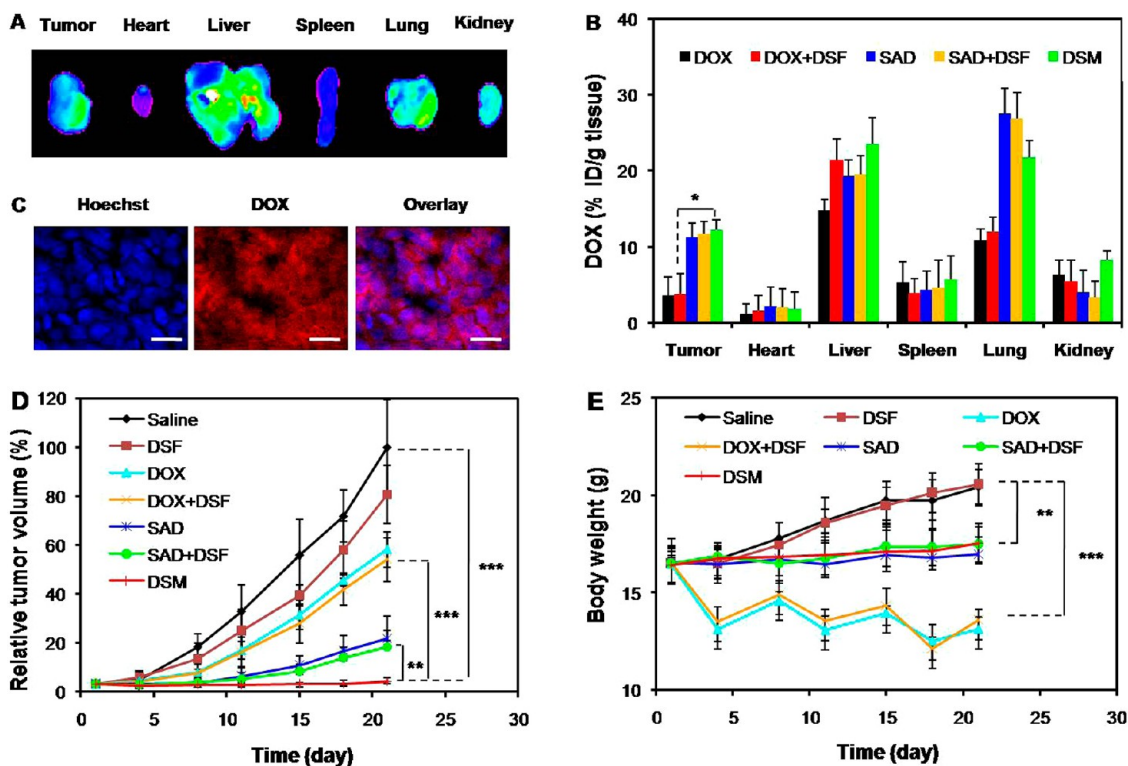
Figure 5. (A) Fluorescence images of tissues and tumor at 4 h after intravenous administration of DSM. (B) Quantitative analysis for the biodistribution of DOX in MCF-7/ADR tumor-bearing mice at 4 h after intravenous administration of DOX, DOX + DSF, SAD, SAD + DSF and DSM. (C) Frozen section of tumor separated from MCF-7/ADR tumor-bearing mice receiving DSM. (Scale bar: 10 $\mu$m). (D) Changes of tumor volume after intravenous injection of saline, DSF, DOX, DOX + DSF, SAD, SAD + DSF and DSM formulations in MCF-7/ADR tumor-bearing nude mice. (E) Body weight changes of MCF-7/ADR tumor-bearing mice after treatment with saline, DSF, DOX, DOX + DSF, SAD, SAD + DSF and DSM formulations. Statistical significance: *$P <$ 0.05, **$P <$ 0.005 and ***$P <$ 0.0005.

**Biodistribution.** The biodistribution of various formulations containing DOX was investigated in MCF-7/ADR tumor model which was generated by injection of 1 × $10^6$ cells in 100 $\mu$L RPMI 1640 medium into the right axilla of female BALB/c nude mice. At 4 h after intravenously administration with DOX, DOX + DSF, SAD, SAD + DSF and DSM at the dose of 10 mg DOX/kg and 2 mg DSF/kg, the tumor-bearing mice were sacrificed, and the heart, liver, spleen, lung, kidney and tumor were excised. The distribution of DOX in each tissue was observed using the FX Pro *in vivo* imaging system (Figure 5A and Figure S11A). DOX, both administrated alone and combined with DSF, showed very low accumulation in tumor, but relatively high accumulation in liver, lung and kidney, suggesting that the combination of DOX with DSF could not promote the tumor uptake of DOX on systemic level. The low concentration in tumor and high content in normal tissue were contributed to the high systematic toxicity of free DOX. On the contrary, the conjugate of DOX, either alone or combined with DSF or co-delivered with DSF, all showed high tumor accumulation, likely due to the enhanced permeability and retention (EPR) effect. Meanwhile, the distribution of DOX was also observed in highly perfused organs, such as liver and lung, because of the high circulating blood passed through

these organs, as well as the unavoidable uptake by the RES in these organs. The biodistribution of DOX was further quantified (Figure 5B). The results were consistent with the fluorescence imaging, showing that the micelles were mainly accumulated in liver and lung, followed by tumor. Specifically, the content of DOX in tumor treated with SAD, SAD + DSF or DSM was about 3-fold of that administrated with DOX alone or combination with DSF. The high tumor accumulation of DOX conjugates would enhance their antitumor effect *in vivo*.

The tumors were further sectioned, stained with Hoechst 33342 and observed under a confocal microscopy for the detailed distribution of DOX in tumor, as reported previously.[33,34] The red fluorescence was barely observed in tumors treated with DOX alone or in combination with DSF, while the red fluorescence was fairly high in that treated with micelles, including SAD, SAD + DSF and DSM (Figure 5C and Figure S11B). In addition, micelles showed wide distribution throughout the tumor tissue, demonstrating increased tissue penetration. The increased penetration and accumulation of micelles in tumor might be attributed to their suitable particle size and negative charged surface, which were beneficial for reduced nonspecific binding, prolonged circulation time, better use of EPR effect and finally the accumulation in tumor.

**In Vivo Antitumor Effect.** To evaluate whether the increased cytotoxicity and improved biodistribution can lead to enhanced therapeutic efficacy, the antitumor efficacy was performed in mice bearing MCF-7/ADR tumor. As shown in Figure 5D and Figure S12, free DOX exhibited a considerable tumor inhibition *in vivo* compared with the control group. At the end of experiment, the tumor volume and tumor weight of free DOX-treated group was 58.12% and 62.40% of control group, respectively. SAD could further improve the inhibitory effect, showing 78.18% and 81.76% reduction in tumor volume and tumor weight at the end of 21 days, respectively. However, the addition of free DSF showed no obvious enhancement in antitumor effect, either in combination with free DOX or SAD, indicating that free DSF could not promote the antitumor effect of DOX on systemic level. When DOX and DSF were co-administrated in DSM, the highest antitumor activity was achieved, with almost completely inhibition of tumor growth. The tumor volume of DSM-treated group was only 4.21% of control group at the end of experiment, which was 12.8-fold and 4.4-fold smaller than that treated with DOX + DSF and SAD + DSF, respectively. In addition, the tumor inhibition rate of DSM was 97.7%, which was significantly higher than that of DOX + DSF (42.6%) and SAD + DSF (85.7%). The superior therapeutic efficacy of DSM could be attributed to the high tumor accumulation of two drugs, increased cellular uptake by tumor cells and the synergistic effect of DOX and DSF on cytotoxicity and apoptosis.

Body weight changes in all mouse groups, as an indicator of systemic toxicity, were measured simultaneously (Figure 5E). The body weight of saline- and DSF-treated mice showed a relatively fast increase, which might be partly due to the fast growth of tumor. Severe weight loss was seen in mice after administration with free DOX alone or in combination with DSF, clearly indicating the serious systemic toxicity of free DOX. Whereas weight in the other groups, including those treated with SAD, SAD + DSF or DSM, did not change greatly, demonstrating the absence of severe systemic toxicity. The cardiotoxicity was further investigated by histopathological analysis and the results were shown in Figure S13. Compared with saline group, obvious accumulation of neutrophils was observed in hearts of mice treated with free DOX and DOX + DSF, indicating that free DOX possessed evident cardiac toxicity, and the combination with free DSF could not decrease the cardiotoxicity of free DOX, perhaps because of its lack of effect on DOX biodistribution. In contrast, no acute pathological change was detected in SAD-, SAD + DSF- and DSM-treated groups, demonstrating that micelles could reduce the cardiac toxicity, probably through reducing the accumulation of DOX in heart. The high antitumor effect, together with the lack of systemic toxicity, suggested that DSM could act as an ideal nanoplatform for the smart co-delivery of chemotherapeutic drugs and MDR modulators into tumors for more effective cancer treatment.

It has been reported that 50−60% of drug development failure is due to insufficient efficacy and ∼20% is due to clinical or preclinical safety.[35,36] Thus, the low therapeutic efficacy with high toxicity is the main problem that need to be solved for medical application. Specifically, the development of MDR is one of main reasons for tumor treatment failure, which will reduce drug accumulation in tumor site and prevent drug from entering tumor cells to exert its therapeutic effect.[37,38] In addition, the physicochemical properties of drug formulations also influence the transport behavior in blood and consequently biodistribution, as well as cellular uptake and trafficking.[9,39] The smart pH-sensitive and temporal-controlled polymeric micelles designed here possessed favorable properties for tumor accumulation and internalization by tumor cells, such as suitable particle size, narrow distribution, negative zeta potential, high stability, temporal release for inhibition of P-gp and drug accumulation in MDR tumor cells. As a result, the smart drug co-delivery system could be promising for medical application due to high therapeutic efficacy with low systemic toxicity.

## CONCLUSION

DSM exhibited a variety of attractive properties in a smart fashion, such as high drug loading with precise drug ratio, long circulation time, improved cellular internalization, and temporal release within tumor cells for inactivation of P-gp and drug accumulation. As a result, DSM could significantly enhance the cytotoxicity of DOX, induce cell apoptosis and change cell cycle. Importantly, DSM showed high tumor accumulation and excellent antitumor effect in MDR tumor with low systemic toxicity. The smart co-delivery system could be the promising intracellular delivery nanovehicles for effective combination therapy.

## MATERIALS AND METHODS

**Materials.** SMA with a molar styrene to maleic anhydride ratio of 1:1 in the backbone (molecular weight 5500 Da) was gifted by Sartomer Company, Inc. (Guangzhou, China). DSF and ADH were obtained from TCI (Shanghai, China). DOX, trypan blue and MTT were purchased from Sigma-Aldrich (St. Louis, MO). Hoechst 33342 and LysoTracker Green were obtained from

Molecular Probes (Eugene, OR). DiO was purchased from Beyotime (Jiangsu, China). Other chemicals if not mentioned were obtained from Sinopharm Group Chemical Reagent Co., Ltd. (Shanghai, China) and were of analytical grade.

**Synthesis and Characterization of SAD Conjugate.** SAD was synthesized through two steps as shown in Figure S1. First, SMA was derivatized with ADH *via* a ring-open reaction between the

hydrazide groups and the maleic anhydride units in the present of triethylamine (TEA) according to the previous method,[40] with a little modification. Briefly, ADH (344.6 mg, 1.98 mmol) and TEA (2 g, 19.8 mmol) dissolved in dimethyl sulfoxide (DMSO) were placed into a round-bottom flask, followed by the dropwise addition of SMA (200 mg, 0.99 mmol of maleic anhydride) in DMSO. The reaction was carried out at room temperature for 24 h with stirring. The reaction mixture was then dialyzed using cellulose dialysis membranes (MWCO: 3.5 kDa, Spectrum Co.) against deionized water for 3 days to remove DMSO and unreacted ADH. After that, water was removed by rotary evaporation, and the polymer SA was dried under vacuum overnight.

Conjugation of DOX to SA was accomplished by formation of a hydrazone between the ketone of DOX and the hydrazide side chain of SA. SA (100 mg, 0.25 mmol of hydrazide) and DOX (71.9 mg, 0.12 mmol) were dissolved in methanol and reacted for 48 h in dark at room temperature. After the reaction was finished, the reaction solution was condensed by rotary evaporation and dialyzed against deionized water. The polymer SAD was centrifugalized, dried under vacuum and obtained as red powder. Conjugation was confirmed by $^1$H NMR spectra recorded on Varian Mercury Plus-400 NMR spectrometer (Varian) operated at 400 MHz. UV scanning spectra were conducted on an UV—vis spectrophotometer (UV-2450, Shimadzu, Japan) to confirm the successful synthesis of SAD conjugate. Elemental analysis was measured on an organic element analyzer (VarioELCUBE, Elementar Analysen systeme GmbH, Germany). The content of DOX in SAD conjugate was determined by fluorescence spectrophotometer (F4600, Hitachi, Japan) with an excitation wavelength of 485 nm and emission wavelength of 590 nm using a standard calibration curve.

The acid degradation of SAD was performed as following, SAD solution was first adjusted to pH 6.0, pH 5.0 or pH 4.0, and then incubated at 37 °C for 2 h. After that, the treated solution was analyzed with Waters HPLC system, equipped with a Waters e2695 separations module, a Waters 2998 photodiode array detector, and a XBridge $C_{18}$ column. HPLC grade methanol/0.1% formic acid (60/40, v/v) was used as the mobile phase at 30 °C with a flow rate of 1.0 mL/min.

**Preparation and Characterization of DSM.** SAD (10 mg) and DSF (1 mg) co-dissolved in 1 mL dimethylformamide (DMF) were dropwise added to 5 mL pure water under vigorous agitation. The micellar solution was then dialyzed against deionized water and filtered with a Millipore filter (pore size: 0.45 $\mu$m) to eliminate unencapsulated DSF. The blank SAD micelles were also prepared as described for DSF-loaded SAD micelles except for the absence of DSF. Size distribution and zeta potential of SAD and DSM were measured by DLS using a Zetasizer (ZS90, Malvern, U.K.) with a scatter angle of 90° at 25 °C. The morphologic examination of micelles was performed by TEM (Tecnai G2 F20 S-TWIN, FEI, Hillsboro, OR) with negative stain method. Before analysis, the samples were stained with 2% (w/v) phosphotungstic acid, and then placed on copper grid with films and air-dried prior to imaging. The colloidal stability of micelles was evaluated in the presence of BSA. Briefly, SAD and DSM diluted in water containing 1%, 5% or 10% BSA were incubated at 37 °C, and the change of micelles size over time was determined by DLS.

The release profile of DSF and DOX from DSM was measured in 0.1 M phosphate buffer solution (PBS, pH 7.4) and 0.1 M acetate buffer solution (ABS, pH 5.0) at 37 °C. In brief, DSM dissolved in PBS or ABS were sealed in a dialysis bag (MWCO: 10 kDa), and immersed in 5 mL of PBS or ABS at 37 °C with continuously shaking (100 rpm). At predetermined time points, all release media were taken out for content measurement and replenished with an equal volume of fresh media. The amount of the released DOX and DSF was measured using fluorescence spectrophotometry and HPLC method, respectively.

**Cell Culture.** MCF-7 and MCF-7/ADR cells, obtained from the American Type Culture Collection (ATCC, Manassas, VA) and Keygen Biotech. Co., Ltd. (Nanjing, China), respectively, were cultured in RPMI 1640 medium containing 10% fetal bovine serum, 100 U/mL penicillin G sodium and 100 $\mu$g/mL streptomycin sulfate at 37 °C and 5% $CO_2$ in a humidified incubator.

Drug resistance of MCF-7/ADR cells was maintained by addition of DOX (1 $\mu$g/mL) in the medium.

**DOX Accumulation and Efflux Assay.** MCF-7 and MCF-7/ADR cells seeded in 24-well plates ($5 \times 10^4$ cells/well) were treated with DOX, DOX + DSF, SAD, SAD + DSF or DSM for 1, 2 and 4 h at 37 °C. The concentrations of DOX and DSF were 5 and 1 $\mu$g/mL, respectively. At the end of experiment, the extracellular fluorescence was quenched with 0.4% trypan blue for 2 min, and cells were then trypsinized, washed three times with ice-cold PBS, resuspended in 500 $\mu$L PBS and measured by FACSCalibur system (BD Biosciences, Oxford, U.K.). The fluorescent intensity was calculated by CellQuest software, and blanked by untreated cells.

To investigate the efflux of DOX, MCF-7 and MCF-7/ADR cells were first treated with DOX, DOX + DSF, SAD, SAD + DSF or DSM (5 $\mu$g DOX/mL and 1 $\mu$g DSF/mL) for 4 h. After washing twice with PBS, cells were further incubated with fresh medium for 1, 2 and 4 h at 37 °C. Then, the extracellular fluorescence was quenched with 0.4% trypan blue for 2 min, and cells were collected and washed with PBS before the DOX retained in cells was determined by FACSCalibur system.

**Subcellular Localization.** MCF-7 and MCF-7/ADR cells were seeded on 10 mm$^2$ glass coverslips placed in 24-well plates and cultured with DOX, DOX + DSF, SAD, SAD + DSF or DSM (5 $\mu$g DOX/mL and 1 $\mu$g DSF/mL) for 3.5 h, followed by staining with Hoechst 33342 and DiO or Hoechst 33342 and Lyso Tracker Green for additional 0.5 h at 37 °C in dark. After the extracellular fluorescence was quenched, cells were washed twice with PBS and fixed with 4% paraformaldehyde for 30 min. Then, cells were mounted on glass slides and visualized using confocal microscope (FluoView TM FV1000, Olympus, Japan).

*In Vitro* Cytotoxicity. MCF-7 and MCF-7/ADR cells seeded in 96-well plates ($1 \times 10^4$ cells/well) were incubated with DSF, DOX, DOX + DSF, SAD, SAD + DSF or DSM at various drug concentrations (mass ratio of DOX to DSF was fixed at 5:1) for 48 h; cell culture supernatants were then harvested and assayed for LDH activity using the LDH release assay kit (Beyotime), according to the manufacturer's protocol. Released LDH were expressed as a percentage of maximum LDH release induced by the incubation of cells with 1% Triton X-100, after normalization to cells treated with corresponding formulations. Meantime, treated cells were further incubated with 200 $\mu$L fresh medium containing 0.5 mg/mL MTT for additional 4 h. After the medium was removed, 150 $\mu$L of DMSO was added to dissolve the crystals formed by living cells. Absorbance at 570 nm was measured using a microplate reader. Cell viability was expressed as a percentage of the absorbance to that of the control experiment without treatment.

**Cell Apoptosis and Cell Cycle Assay.** MCF-7/ADR cells seeded in 12-well plates ($1 \times 10^5$ cells/well) were treated with DSF, DOX, DOX + DSF, SAD, SAD + DSF or DSM (5 $\mu$g DOX/mL and 1 $\mu$g DSF/mL) for 48 h, and then stained with Hoechst 33342 at 37 °C for 30 min in dark. The cellular and nuclear morphology was observed using a fluorescence inversion microscope (IX81, Olympus, Japan). For quantitative measurement of apoptosis, treated cells were harvested, washed twice with ice-cold PBS, stained with Annexin V-FITC and PI for 15 min at room temperature in the dark, and then analyzed by FACSCalibur system. For cell cycle assay, treated cells were collected, washed twice with ice-cold PBS, fixed with 70% ethanol at 4 °C overnight and treated with RNase A for 45 min, followed by PI staining for 30 min. The alteration of cell cycle was analyzed by FACSCalibur system.

**Animals and Tumor Model.** Adult Sprague—Dawley rats (200 ± 20 g) and female BALB/c nude mice aged 5 weeks (16—20 g) were supplied by Shanghai Experimental Animal Center and kept under a 12 h light/dark cycle at the Animal Care Facility. The animals were given daily fresh diet with free access to water and acclimatized for at least 5 days prior to the experiments. The *in vivo* experiments were carried out under the guideline approved by the Institutional Animal Care and Use Committee (IACUC) of the Shanghai Institute of Materia Medica, Chinese Academy of Sciences. Subcutaneous tumor model was generated by injection of $1 \times 10^6$ MCF-7/ADR cells into the right axilla of nude mice. The tumors were allowed to grow to ~100 mm$^3$ before experiment.

*In Vivo* Pharmacokinetics. Sprague—Dawley rats were randomly divided into six groups, and injected intravenously with

DSF, DOX, DOX + DSF, SAD, SAD + DSF and DSM, respectively, at the dose of 10 mg DOX/kg and 2 mg DSF/kg. Approximately 0.5 mL of blood samples was collected in a heparinized tube from the orbital venous plexus at 5, 15, and 30 min, and 1, 2, 4, 6, 8, 10, and 24 h post injection and immediately centrifuged at 5000 rpm for 10 min to harvest plasma samples. Drugs were extracted from plasma by deproteinization using acetonitrile, followed by centrifugation at 10 000 rpm for 10 min. The content of DOX and DSF in supernatant was then measured by fluorescence spectrophotometry and HPLC method, respectively.

**Biodistribution.** To assess the tissue distribution of DOX formulations, the MCF-7/ADR tumor-bearing mice were intravenously injected *via* tail vein with DOX, DOX + DSF, SAD, SAD + DSF and DSM at the dose of 10 mg DOX/kg and 2 mg DSF/kg, respectively. Mice were sacrificed at 4 h after administration, and the heart, liver, spleen, lung, kidney and tumor were excised, washed with cold saline and observed using the FX Pro *in vivo* imaging system (Carestream Health). For quantitative analysis, tissue samples were then homogenized in 0.5 mL acetonitrile, followed by centrifugation at 10 000 rpm for 10 min. The content of DOX in each tissue was measured using fluorescence spectrophotometry, and expressed as percentage of the injected dose per gram of tissue (%ID/g tissue). To investigate the detail of DOX distribution in tumor site, the tumor was sectioned at 5 $\mu$m thickness using cryostat microtome (SLEE, Mainz, Germany), and stained with Hoechst 33342 for confocal microscopy observation.

**In Vivo Antitumor Effect.** Mice bearing MCF-7/ADR tumor were randomly divided into seven groups ($n = 6$) and administrated intravenously once a week with saline, DSF, DOX, DOX + DSF, SAD, SAD + DSF or DSM for three weeks at the dose of 10 mg DOX/kg and 2 mg DSF/kg, respectively. Body weight and tumor volume ([major axis] $\times$ [minor axis]$^2$/2, measured by calipers) were monitored and recorded twice a week over a period of 21 days. Tumor volume of saline-treated group on day 21 was normalized to 100% for all groups. At the end of experiment, mice were sacrificed, and tumors were excised, weighted and photographed. In addition, the hearts were also collected, fixed in 10% formalin and embedded in paraffin; the paraffin-embedded tissues were then sectioned at 5 $\mu$m thickness and stained with hematoxylin and eosin (H&E) for histopathological analysis.

**Statistical Analysis.** All values were expressed as mean $\pm$ SD and each value was the mean of at least three repetitive experiments in each group. Nonparametric test was performed using IBM SPSS statistics to assess the significance of the difference between two groups.

*Conflict of Interest:* The authors declare no competing financial interest.

*Supporting Information Available:* Additional tables and figures as described in the text. Synthesis and characterization of SAD conjugate, physical properties of SAD micelles, intracellular localization, IC$_{50}$ and LD$_{50}$ values of various drug formulations, cell apoptosis, cell cycle, pharmacokinetic parameters, biodistribution, tumor picture, tumor weight and cardiotoxicity examination. This material is available free of charge *via* the Internet at http://pubs.acs.org.

## REFERENCES AND NOTES

1. Woodcock, J.; Griffin, J. P.; Behrman, R. E. Development of Novel Combination Therapies. *N. Engl. J. Med.* **2011**, *364*, 985–987.
2. Jabr-Milane, L. S.; van Vlerken, L. E.; Yadav, S.; Amiji, M. M. Multi-functional Nanocarriers to Overcome Tumor Drug Resistance. *Cancer Treat. Rev.* **2008**, *34*, 592–602.
3. Hu, C.-M. J.; Aryal, S.; Zhang, L. Nanoparticle-Assisted Combination Therapies for Effective Cancer Treatment. *Ther. Delivery* **2010**, *1*, 323–334.
4. Lehar, J.; Krueger, A. S.; Avery, W.; Heilbut, A. M.; Johansen, L. M.; Price, E. R.; Rickles, R. J.; Short, G. F., III; Staunton, J. E.; Jin, X.; *et al.* Synergistic Drug Combinations Tend to Improve Therapeutically Relevant Selectivity. *Nat. Biotechnol.* **2009**, *27*, 659–666.
5. Hu, C.-M. J.; Zhang, L. Nanoparticle-based Combination Therapy toward Overcoming Drug Resistance in Cancer. *Biochem. Pharmacol.* **2012**, *83*, 1104–1111.
6. Greco, F.; Vicent, M. J. Combination Therapy: Opportunities and Challenges for Polymer–Drug Conjugates as Anti-cancer Nanomedicines. *Adv. Drug Delivery Rev.* **2009**, *61*, 1203–1213.
7. Kolishetti, N.; Dhar, S.; Valencia, P. M.; Lin, L. Q.; Karnik, R.; Lippard, S. J.; Langer, R.; Farokhzad, O. C. Engineering of Self-assembled Nanoparticle Platform for Precisely Controlled Combination Drug Therapy. *Proc. Natl. Acad. Sci. U.S.A.* **2010**, *107*, 17939–17944.
8. Chen, H.; Pazicni, S.; Krett, N. L.; Ahn, R. W.; Penner-Hahn, J. E.; Rosen, S. T.; O'Halloran, T. V. Coencapsulation of Arsenic- and Platinum-based Drugs for Targeted Cancer Treatment. *Angew. Chem., Int. Ed.* **2009**, *48*, 9295–9299.
9. Duan, X. P.; Li, Y. P. Physicochemical Characteristics of Nanoparticles Affect Circulation, Biodistribution, Cellular Internalization, and Trafficking. *Small* **2013**, *9*, 1521–1532.
10. Kastantin, M.; Missirlis, D.; Black, M.; Ananthanarayanan, B.; Peters, D.; Tirrell, M. Thermodynamic and Kinetic Stability of DSPE-PEG(2000) Micelles in the Presence of Bovine Serum Albumin. *J. Phys. Chem. B* **2010**, *114*, 12632–12640.
11. Dong, H.; Dube, N.; Shu, J. Y.; Seo, J. W.; Mahakian, L. M.; Ferrara, K. W.; Xu, T. Long-Circulating 15 nm Micelles Based on Amphiphilic 3-Helix Peptide-PEG Conjugates. *ACS Nano* **2012**, *6*, 5320–5329.
12. Xiao, K.; Li, Y.; Luo, J.; Lee, J. S.; Xiao, W.; Gonik, A. M.; Agarwal, R. G.; Lam, K. S. The Effect of Surface Charge on *in vivo* Biodistribution of PEG-Oligocholic Acid Based Micellar Nanoparticles. *Biomaterials* **2011**, *32*, 3435–3446.
13. Loo, T. W.; Bartlett, M. C.; Clarke, D. M. Disulfiram Metabolites Permanently Inactivate the Human Multidrug Resistance P-glycoprotein. *Mol. Pharmaceutics* **2004**, *1*, 426–433.
14. Loo, T. W.; Clarke, D. M. Blockage of Drug Resistance *in vitro* by Disulfiram, A Drug Used To Treat Alcoholism. *J. Natl. Cancer Inst.* **2000**, *92*, 898–902.
15. Regev, R.; Yeheskely-Hayon, D.; Katzir, H.; Eytan, G. D. Transport of Anthracyclines and Mitoxantrone Across Membranes by A Flip-Flop Mechanism. *Biochem. Pharmacol.* **2005**, *70*, 161–169.
16. Krylova, O. O.; Melik-Nubarov, N. S.; Badun, G. A.; Ksenofontov, A. L.; Menger, F. M.; Yaroslavov, A. A. Pluronic L61 Accelerates Flip-Flop and Transbilayer Doxorubicin Permeation. *Chem.—Eur. J.* **2003**, *9*, 3930–3936.
17. Decorti, G.; Peloso, I.; Favarin, D.; Klugmann, F. B.; Candussio, L.; Crivellato, E.; Mallardi, F.; Baldini, L. Handling of Doxorubicin by the LLC-PK1 Kidney Epithelial Cell Line. *J. Pharmacol. Exp. Ther.* **1998**, *286*, 525–530.
18. Regev, R.; Eytan, G. D. Flip-Flop of Doxorubicin across Erythrocyte and Lipid Membranes. *Biochem. Pharmacol.* **1997**, *54*, 1151–1158.
19. Hillaireau, H.; Couvreur, P. Nanocarriers' Entry into the Cell: Relevance to Drug Delivery. *Cell. Mol. Life Sci.* **2009**, *66*, 2873–2896.
20. Fernando, L. P.; Kandel, P. K.; Yu, J.; McNeill, J.; Ackroyd, P. C.; Christensen, K. A. Mechanism of Cellular Uptake of Highly Fluorescent Conjugated Polymer Nanoparticles. *Biomacromolecules* **2010**, *11*, 2675–2682.
21. Nam, H. Y.; Kwon, S. M.; Chung, H.; Lee, S.-Y.; Kwon, S.-H.; Jeon, H.; Kim, Y.; Park, J. H.; Kim, J.; Her, S.; *et al.* Cellular Uptake Mechanism and Intracellular Fate of Hydrophobically Modified Glycol Chitosan Nanoparticles. *J. Controlled Release* **2009**, *135*, 259–267.
22. Wang, F.; Wang, Y.-C.; Dou, S.; Xiong, M.-H.; Sun, T.-M.; Wang, J. Doxorubicin-Tethered Responsive Gold Nanoparticles Facilitate Intracellular Drug Delivery for Overcoming Multidrug Resistance in Cancer Cells. *ACS nano* **2011**, *5*, 3679–3692.

23. Pentassuglia, L.; Graf, M.; Lane, H.; Kuramochi, Y.; Cote, G.; Timolati, F.; Sawyer, D. B.; Zuppinger, C.; Suter, T. M. Inhibition of ErbB2 by Receptor Tyrosine Kinase Inhibitors Causes Myofibrillar Structural Damage without Cell Death in Adult Rat Cardiomyocytes. *Exp. Cell Res.* **2009**, *315*, 1302–1312.

24. Chen, D.; Cui, Q. C.; Yang, H.; Dou, Q. P. Disulfiram, A Clinically Used Anti-alcoholism Drug and Copper-binding Agent, Induces Apoptotic Cell Death in Breast Cancer Cultures and Xenografts *via* Inhibition of the Proteasome Activity. *Cancer Res.* **2006**, *66*, 10425–10433.

25. Lövborg, H.; Öberg, F.; Rickardson, L.; Gullbo, J.; Nygren, P.; Larsson, R. Inhibition of Proteasome Activity, Nuclear Factor-κB Translocation and Cell Survival by the Antialcoholism Drug Disulfiram. *Int. J. Cancer* **2006**, *118*, 1577–1580.

26. Yip, N. C.; Fombon, I. S.; Liu, P.; Brown, S.; Kannappan, V.; Armesilla, A. L.; Xu, B.; Cassidy, J.; Darling, J. L.; Wang, W. Disulfiram Modulated ROS-MAPK and NF-κB Pathways and Targeted Breast Cancer Cells with Cancer Stem Cell-like Properties. *Br. J. Cancer* **2011**, *104*, 1564–1574.

27. Morrison, B. W.; Doudican, N. A.; Patel, K. R.; Orlow, S. J. Disulfiram Induces Copper-dependent Stimulation of Reactive Oxygen Species and Activation of the Extrinsic Apoptotic Pathway in Melanoma. *Melanoma Res.* **2010**, *20*, 11–20.

28. Wang, W.; McLeod, H. L.; Cassidy, J. Disulfiram-Mediated Inhibition of NF-κB Activity Enhances Cytotoxicity of 5-Fluorouracil in Human Colorectal Cancer Cell Lines. *Int. J. Cancer* **2003**, *104*, 504–511.

29. Guo, X.; Xu, B.; Pandey, S.; Goessl, E.; Brown, J.; Armesilla, A. L.; Darling, J. L.; Wang, W. Disulfiram/Copper Complex Inhibiting NF-κB Activity and Potentiating Cytotoxic Effect of Gemcitabine on Colon and Breast Cancer Cell Lines. *Cancer Lett.* **2010**, *290*, 104–113.

30. Pozza, E. D.; Donadelli, M.; Costanzo, C.; Zaniboni, T.; Dando, I.; Franchini, M.; Arpicco, S.; Scarpa, A.; Palmieri, M. Gemcitabine Response in Pancreatic Adenocarcinoma Cells Is Synergistically Enhanced by Dithiocarbamate Derivatives. *Free Radical Biol. Med.* **2011**, *50*, 926–933.

31. Xu, B.; Shi, P.; Fombon, I. S.; Zhang, Y.; Huang, F.; Wang, W.; Zhou, S. Disulfiram/Copper Complex Activated JNK/c-jun Pathway and Sensitized Cytotoxicity of Doxorubicin in Doxorubicin Resistant Leukemia HL60 Cells. *Blood Cells, Mol., Dis.* **2011**, *47*, 264–269.

32. Reinhardt, H. C.; Hasskamp, P.; Schmedding, I.; Morandell, S.; van Vugt, M. A. T. M.; Wang, X.; Linding, R.; Ong, S.-E.; Weaver, D.; Carr, S. A.; *et al.* DNA Damage Activates A Spatially Distinct Late Cytoplasmic Cell-Cycle Checkpoint Network Controlled by MK2-Mediated RNA Stabilization. *Mol. Cell* **2010**, *40*, 34–49.

33. Huang, S.; Shao, K.; Liu, Y.; Kuang, Y.; Li, J.; An, S.; Guo, Y.; Ma, H.; Chen, J. Tumor-Targeting and Microenvironment-Responsive Smart Nanoparticles for Combination Therapy of Antiangiogenesis and Apoptosis. *ACS Nano* **2013**, *7*, 2860–2871.

34. Li, L.; Guan, Y.; Liu, H.; Hao, N.; Liu, T.; Meng, X.; Fu, C.; Li, Y.; Qu, Q.; Zhang, Y.; *et al.* Silica Nanorattle-Doxorubicin-Anchored Mesenchymal Stem Cells for Tumor-Tropic Therapy. *ACS Nano* **2011**, *5*, 7462–7470.

35. Arrowsmith, J. Trial Watch: Phase II Failures: 2008−2010. *Nat. Rev. Drug Discovery* **2011**, *10*, 328–329.

36. Arrowsmith, J. Trial Watch: Phase III and Submission Failures: 2007−2010. *Nat. Rev. Drug Discovery* **2011**, *10*, 87–87.

37. Szakacs, G.; Paterson, J. K.; Ludwig, J. A.; Booth-Genthe, C.; Gottesman, M. M. Targeting Multidrug Resistance in Cancer. *Nat. Rev. Drug Discovery* **2006**, *5*, 219–234.

38. Eckhardt, B. L.; Francis, P. A.; Parker, B. S.; Anderson, R. L. Strategies for the Discovery and Development of Therapies for Metastatic Breast Cancer. *Nat. Rev. Drug Discovery* **2012**, *11*, 479–497.

39. Adiseshaiah, P. P.; Hall, J. B.; McNeil, S. E. Nanomaterial Standards for Efficacy and Toxicity Assessment. *Wiley Interdiscip. Rev.: Nanomed. Nanobiotechnol.* **2009**, *2*, 99–112.

40. Duan, X. P.; Xiao, J. S.; Yin, Q.; Zhang, Z. W.; Mao, S. R.; Li, Y. P. Amphiphilic Graft Copolymer Based on Poly(styrene-co-maleic anhydride) with Low Molecular Weight Polyethylenimine for Efficient Gene Delivery. *Int. J. Nanomed.* **2012**, *7*, 4961–4972.